



PCCP

Structural Stability, Dihydrogen Bonding, and Pressure-Induced Polymorphic Transformations in Hydrazine Borane

| | |
|-------------------------------|---|
| Journal: | <i>Physical Chemistry Chemical Physics</i> |
| Manuscript ID | CP-ART-03-2023-001301.R1 |
| Article Type: | Paper |
| Date Submitted by the Author: | 11-Jun-2023 |
| Complete List of Authors: | Guan, Rongfeng; Western University, Department of Chemistry Wang, Pan; University of Western Ontario, Department of Chemistry Ji, Yujin; Soochow University, Institute of Functional Nano & Soft Materials (FUNSOM) Li, Youyong; Soochow University, Institute of Functional Nano & Soft Materials (FUNSOM) Song, Yang; Western University, Department of Chemistry |
| | |

SCHOLARONE™
Manuscripts

Structural Stability, Dihydrogen Bonding, and Pressure-Induced Polymorphic Transformations in Hydrazine Borane

Rongfeng Guan,^{ab} Pan Wang,^a Yujin Ji,^{*b} Youyong Li,^{bc} and Yang Song^{*ac}

^a*Department of Chemistry, The University of western Ontario, London, Ontario, N6A 5B7, Canada*

^b*Institute of Functional Nano & Soft Materials (FUNSOM), Jiangsu Key Laboratory for Carbon-Based Functional Materials and Devices, Soochow University, Suzhou 215123, Jiangsu, China*

^c*Soochow University – Western University Centre for Synchrotron Radiation Research, The University of Western Ontario, London, ON N6A 5B7, Canada*

Abstract

Hydrazine borane ($\text{N}_2\text{H}_4\text{BH}_3$) has attracted considerable interest as a promising solid-state hydrogen storage material owing to its high hydrogen content and easy preparation. In this work, pressure-induced phase transitions of $\text{N}_2\text{H}_4\text{BH}_3$ were investigated using a combination of vibrational spectroscopy, X-ray diffraction, and density functional theory (DFT) up to 30 GPa. Our results showed that $\text{N}_2\text{H}_4\text{BH}_3$ exhibits remarkable structural stability in a very broad pressure region up to 15 GPa, and then two phase transitions were identified: the first one is from the ambient-pressure *Pbcn* phase to a *Pbca* phase near 15 GPa; the second is from the *Pbca* phase to a *Pccn* phase near 25 GPa. As revealed by DFT calculations, the unusual stability of $\text{N}_2\text{H}_4\text{BH}_3$ and the late phase transformations were attributed to the pressure-mediated evolutions of dihydrogen bonding frameworks, the compressibility as well as enthalpies of high-pressure polymorphs. Our findings provide new insight into the structures and bonding properties of $\text{N}_2\text{H}_4\text{BH}_3$ that are important for hydrogen storage applications.

1. Introduction

Development of effective hydrogen storage materials is the key to promote the use of hydrogen as a clean energy source. Over the past several decades, solid-state hydrogen storage materials with high gravimetric and high volumetric hydrogen density have been extensively studied to fully understand the related mechanisms and to improve the efficiency of hydrogen storage/release properties to applications.⁽²⁾ Ammonia borane (NH_3BH_3) is a very well-studied promising hydrogen storage material due to its very high hydrogen content (19.6 wt %) and stability under ambient conditions.⁽³⁾ One of the most important findings by the extensive studies of NH_3BH_3 is the dihydrogen bonding, $\text{N}-\text{H}\cdots\text{H}-\text{B}$, which contributes to the structural stability and the dehydrogenation performance of NH_3BH_3 .⁽⁴⁾⁻⁽⁶⁾ Moreover, high-pressure studies on NH_3BH_3 revealed that pressure can tune structures and thus the dehydrogenation performance on NH_3BH_3 , and even lead to the formation of novel hydrogen storage materials upon compression.⁽⁷⁾⁻⁽¹⁴⁾ However, NH_3BH_3 still faces multiple challenges in its practical application as a hydrogen storage material, such as slow decomposition kinetics, relatively high reaction starting temperature, and harmful by-products that damage the fuel cells.⁽¹⁵⁾ Therefore, searching for alternatives of NH_3BH_3 to address these issues represents an important theme in the development of hydrogen storage materials.

Hydrazine borane ($\text{N}_2\text{H}_4\text{BH}_3$) as a derivative of NH_3BH_3 is a particularly promising hydrogen storage material with high hydrogen content (15.4 wt %) and can be synthesized via the reaction of hydrazinium sulfate with sodium borohydride in cyclic ethers.⁽¹⁶⁾⁻⁽¹⁸⁾ The dehydrogenation of $\text{N}_2\text{H}_4\text{BH}_3$ can be approached by either hydrolysis or thermolysis, and the hydrogen release rate of $\text{N}_2\text{H}_4\text{BH}_3$ can be significantly improved by adding lithium hydride in a temperature range of 100–150°C.⁽¹⁹⁾ Similar to the studies on NH_3BH_3 , the application of external pressure can have

significant effects on $\text{N}_2\text{H}_4\text{BH}_3$ by modifying the crystal structures and dihydrogen bonding behaviours. In particular, one of the major aspects for investigating hydrogen storage materials under high pressure involves the access to and characterization of new stable or metastable phases.^{(7),(11),(13),(20)-(23)} Yot et al.⁽²⁴⁾ reported the structural behaviors of $\text{N}_2\text{H}_4\text{BH}_3$ under pressures up to 2 GPa using synchrotron X-ray diffraction (XRD) aided with density functional theory (DFT) calculations. However, only simple contraction in unit cell dimension was found, but no phase transitions were observed at pressures up to 2 GPa, which is the highest pressure achieved. The possibility of the structural transformation of $\text{N}_2\text{H}_4\text{BH}_3$ and the evolution of dihydrogen bonds in the higher-pressure region which are the key to stabilizing the structure and hydrogen release kinetics of $\text{N}_2\text{H}_4\text{BH}_3$, are still unknown and thus require further investigation.

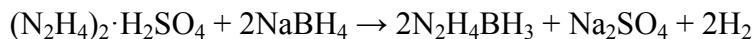
In this study, we systematically investigate the pressure-induced structural transformation of $\text{N}_2\text{H}_4\text{BH}_3$ upon compression to ~ 30 GPa using a combination of *in situ* IR spectroscopy, Raman spectroscopy, synchrotron X-ray diffraction, and DFT calculations. Our findings show the unique high structural stability of $\text{N}_2\text{H}_4\text{BH}_3$ in the pressure range of 0–15 GPa and reveal two new possible phase transitions at higher pressures. These findings provide useful information on pressure-tune structures and bonding related to the mechanism of the dehydrogenation process of $\text{N}_2\text{H}_4\text{BH}_3$ as a promising hydrogen storage material.

2. Experimental and computational methods

2.1 Sample Preparation

Hydrazine hemisulfate (N_2H_4) $\cdot\text{H}_2\text{SO}_4$ (98%), sodium borohydride NaBH_4 (98%), and anhydrous 1,4-dioxane (99.8%) were purchased from Sigma Aldrich with claimed purity and used

as received. $\text{N}_2\text{H}_4\text{BH}_3$ crystal was synthesized based on the previously reported method by the following reaction.⁽¹⁷⁾



4.86 g $(\text{N}_2\text{H}_4)_2\cdot\text{H}_2\text{SO}_4$ (0.03 mol) and 2.27 g NaBH_4 (0.06 mol) were ground into fine powders separately in a mortar of a glovebox, followed by transferring into a 100 mL round bottom flask. 50 mL of dioxane was then added to the flask and the reaction occurred immediately once they were mixed. The flask was placed into an oil bath and the temperature was set at 30 °C. After the mixture was stirred for 48 hours under 30 °C, the suspension was filtered and the solid was washed with 50 mL of dioxane. Lastly, the filtrate was under the vacuum to remove the solvent. The final product is a white solid, which was dried under vacuum and room temperature overnight. The product was kept in an N_2 -filled MBraun LAB Master 130 glovebox with H_2O content of < 1 ppm and O_2 content of < 3 ppm.

2.2 Structural Characterizations

The crystallinity and purity of the as-synthesized product were tested by a Rigaku X-ray diffractometer using Co $\text{K}\alpha$ radiation ($\lambda = 1.78890 \text{ \AA}$), the scan range was from $2\theta = 10$ to 80° with a step size of 0.02. The sample was covered by a piece of Kapton film during the measurement to avoid moisture. The diffraction pattern was refined by the Rietveld method using GSAS-II software⁽²⁵⁾⁽²⁵⁾Error! Reference source not found. (Fig. S1†).

A symmetrical diamond anvil cell with two type II diamonds with a culet size of 400 μm was used for IR measurement. A stainless-steel gasket with a thickness of 40 μm and a 130 μm hole in the center served as the sample chamber. A ruby ball and a small amount of KBr were pre-loaded into the sample chamber, followed by the loading of the sample in the glovebox. The main parts

of the IR micro-spectroscopy system include a commercial Fourier transform infrared (FTIR) spectrometer from Bruker Optics Inc. (model Vertex 80v) and a Global IR light source. The system is operated under a vacuum of less than 5 mbar in order to remove the interference from H₂O and CO₂. An IR beam is collimated and directed into a relay box through a KBr window on the spectrometer. The beam is then focused onto the sample by iris optics and 15× reflective objective lens. After the DAC is placed on the sample stage and aligned with the aid of an optical microscope, the size of the IR beam is adjusted to be identical to the sample size by a series of iris apertures. Then the transmitted IR beam is collected and reflected by a condenser and several mirrors and directed to a midband mercury cadmium telluride (MCT) detector allowing measurements in the spectral range of 600 cm⁻¹ to 12000 cm⁻¹. A reference spectrum was collected as the background, which is the spectrum of diamonds and KBr loaded in the sample hole. Subsequently, the spectrum of each sample could be collected with a resolution of 4 cm⁻¹ and 512 scans.

For Raman spectroscopy measurements, a symmetrical diamond anvil cell with two type I diamonds with a culet size of 400 μm was used. The *in situ* high-pressure Raman experiments were carried out by a customized Raman spectrometer with a 532 nm diode pumped solid state laser as the excitation source. A spectrometer (SpectroPro-2500i, Acton Research Corporation) equipped with a grating of 1200 lines/mm was used for all measurements. The Raman spectrum is recorded by a charge-coupled device (CCD) detector (Spec-10 from Princeton Instrument), which is cooled by liquid nitrogen to maintain the -120 °C operation condition. The system is calibrated by using standard neon lines with the resolution of ± 1 cm⁻¹.

A symmetrical diamond anvil cell with two type I diamonds with the culet size of 400 μm was used for high-pressure synchrotron XRD study. The sample was loaded into the sample chamber

with a ruby ball as a pressure calibrant in the glovebox. No pressure-transmitting medium was used due to the sensitivity and reactivity of the sample. The in situ high-pressure XRD patterns were collected at beamline 20ID at Advanced Photon Source (APS) of Argonne National Laboratory (ANL). CeO₂ was used as a calibrant to determine the diffraction geometry of the synchrotron XRD setup at the Sector 20. The wavelength of the monochromatic X-ray beam is 0.4592 Å. The 2D Debye-Scherrer diffraction patterns were collected using a MARCCD detector and integrated by using Fit2D or Dioptas programs for further analysis. The integrated 1D XRD patterns are analyzed by Rietveld refinement using GSAS-II software.⁽²⁵⁾

2.3 Computational Methodology

First-principles calculations based on DFT were performed using the CASTEP⁽²⁶⁾ program (Version 20.1.1). The lattice parameters of the high-pressure N₂H₄BH₃ structures were optimized at the target pressure by minimizing the enthalpy. The known structure of N₂H₄BH₃ at ambient conditions was used for selecting the exchange-correlation functional, pseudopotentials, k-mesh sampling, and kinetic energy cutoff.⁽²⁷⁾ High-pressure candidate structures of N₂H₄BH₃ were generated using the USPEX evolutionary search program.^{(28),(29)} The resulting candidate structures were optimized using the Perdew–Burke–Ernzerhof⁽³⁰⁾Error! Reference source not found. (PBE) generalized gradient approximation, including PBE ultrasoft pseudopotentials with a kinetic energy cutoff of 800 eV. The Monkhorst–Pack method⁽³¹⁾ was used for Brillouin zone sampling with the following k-point meshes for the following 5 final candidate structures: 4 × 9 × 5 (*Pbcn*), 4 × 9 × 5 (*Pbca*), 3 × 6 × 9 (*Pcca*), 2 × 6 × 5 (*Pmc2₁*), 5 × 3 × 8 for *Pccn* (A), and 4 × 5 × 6 for *Pccn* (B). All the structures are fully optimized without any symmetry constraints until the energy tolerances less than 0.001 eV per atom, and the force is smaller than 0.003 eV/Å. The convergence threshold of 1.0 × 10⁻⁹ eV/atom is selected in the self-consistent field (SCF) calculations. The

$\text{N}_2\text{H}_4\text{BH}_3$ structures identified as phases I–III were verified to be true minima by phonon calculations. All the calculations correspond to $T = 0$ K.

3. Results and Discussion

3.1 IR and Raman vibrational modes of $\text{N}_2\text{H}_4\text{BH}_3$ at high pressures up to 15 GPa.

As a starting point, the IR and Raman spectra of $\text{N}_2\text{H}_4\text{BH}_3$ were collected under ambient pressure at room temperature (Fig. 1). Consistent with the molecular structure of $\text{N}_2\text{H}_4\text{BH}_3$, the most characteristic vibrational bands were observed, including the N–H stretching region (2600 to 3400 cm^{-1}), the B–H stretching region (2200 to 2500 cm^{-1}), the N–H asymmetric bending region (1590 to 1630 cm^{-1}), and the B–H bending region (1100 to 1300 cm^{-1}) as well as the lattice region (Table S1†). Subsequently, we collected the *in situ* IR and Raman spectra of $\text{N}_2\text{H}_4\text{BH}_3$ upon compression up to 15 GPa (Fig. S2, S3†), significantly beyond the previously investigated pressure region (i.e., < 2 GPa). Both the IR and Raman spectra of $\text{N}_2\text{H}_4\text{BH}_3$ upon compression revealed that all the vibrational modes gradually and continuously shifted towards higher frequency until the highest pressure of ~ 15 GPa, where significant profile broadening observed suggests pressure-induced structural disorder. No prominent change in the spectroscopic profiles of the vibrational modes was observed in the entire compression region, indicating the absence of phase transition and thus the high structural stability of $\text{N}_2\text{H}_4\text{BH}_3$. This observation is in strong contrast to the extensively studied NH_3BH_3 , which has been shown to exhibit rich pressure-induced phase transitions such as at around 1.2, 11.0, and 20.0 GPa.⁽³²⁾ Similarly, other NH_3BH_3 derivatives, such as ethylenediamine bisborane, has also been reported to have pressure-induced phase transitions even in a much lower pressure region, such as at about 1.0 and 7.0 GPa.⁽²³⁾

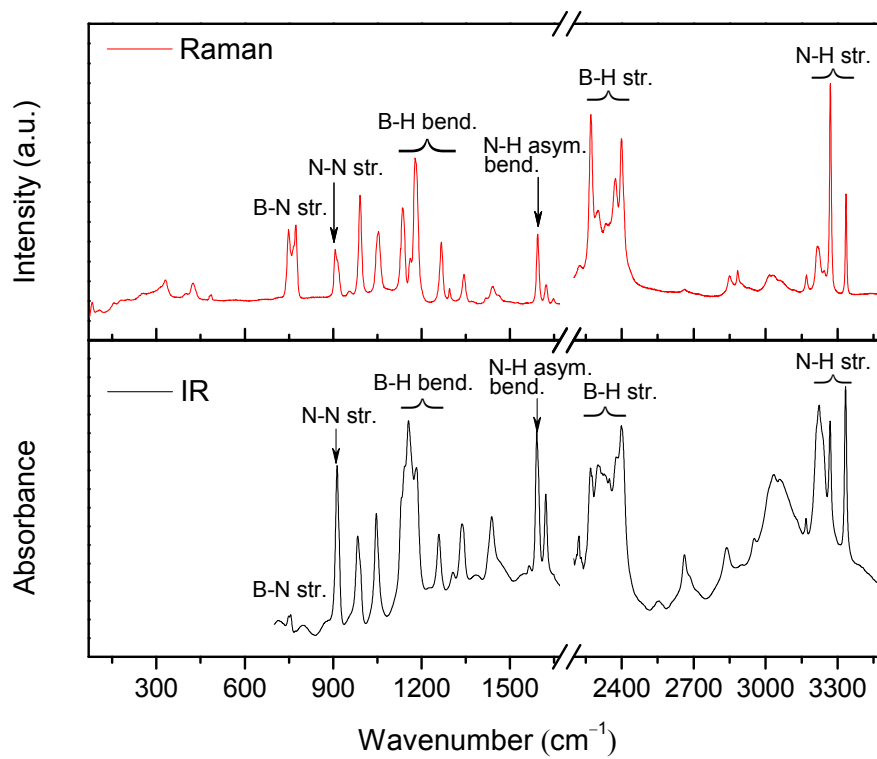
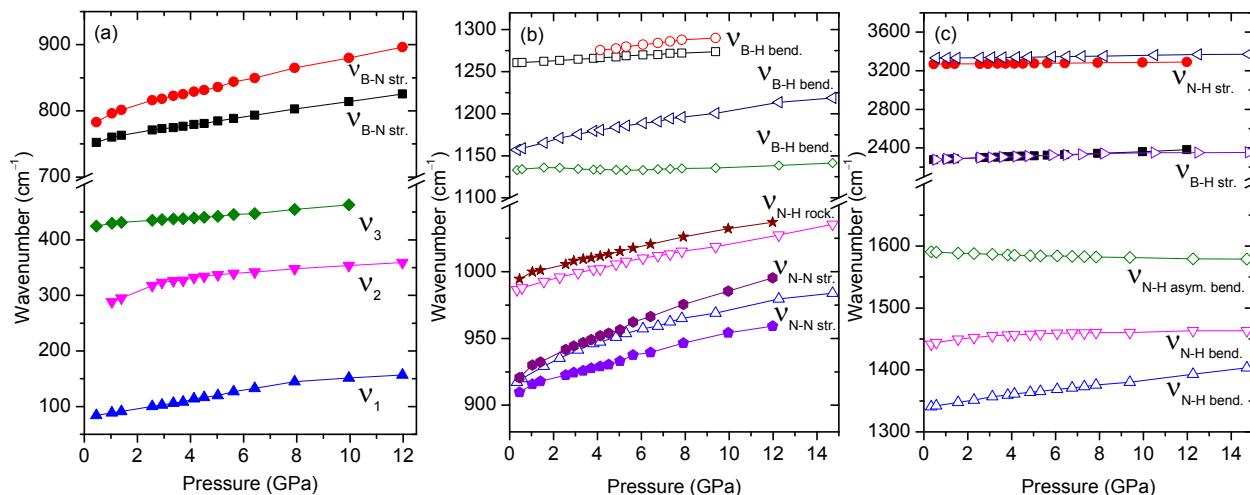


Fig 1. Raman and IR spectra of $\text{N}_2\text{H}_4\text{BH}_3$ collected at room temperature under ambient pressure.

To verify the structural stability of $\text{N}_2\text{H}_4\text{BH}_3$, the shift of vibrational modes as a function of pressure was further examined, as shown in Fig. 2 with the detailed pressure dependence of



selected IR and Raman modes on compression shown in Tables S2 and S3. As expected, most of the vibrational modes exhibit blueshift due to the stiffening of most chemical bonds under high pressure. Compared to other compounds in the NH_3BH_3 family, such as itself and ethylenediamine bisborane, the evolution of N–H bonds in $\text{N}_2\text{H}_4\text{BH}_3$ under high pressure shows the significant difference. In particular, the frequency of N–H bonds in NH_3BH_3 shows obvious redshifts upon compression, indicating the pressure-induced strengthening of the dihydrogen bonding $\text{N-H}\cdots\text{H-B}$. However, the frequency of N–H bonds in $\text{N}_2\text{H}_4\text{BH}_3$ shows no redshift in any Raman modes and only a minor redshift in the N-H asymmetric IR bending mode (Fig. 2c and Table S2), indicating pressure plays a significantly different role in structural evolution of $\text{N}_2\text{H}_4\text{BH}_3$ than in other NH_3BH_3 derivatives.

Fig. 2. Pressure dependence of selected Raman (solid symbols) and IR (open symbols) modes of $\text{N}_2\text{H}_4\text{BH}_3$.

3.2 X-ray diffraction patterns of $\text{N}_2\text{H}_4\text{BH}_3$ at high pressure up to 20 GPa.

The XRD pattern of $\text{N}_2\text{H}_4\text{BH}_3$ collected under ambient conditions as a starting point (Fig. S1†) can be well indexed and refined using the previously published orthorhombic structure with a $Pbcn$ space group.⁽¹⁶⁾ The refined unit cell parameters are $a = 13.108 \text{ \AA}$, $b = 5.099 \text{ \AA}$, $c = 9.590 \text{ \AA}$, and V

= 637.880 Å³, which are consistent to the references.^{(16),(24)} To gain insight into the pressure effect on the structure of N₂H₄BH₃, we then collected the synchrotron XRD patterns of N₂H₄BH₃ from near ambient pressure to 20 GPa at room temperature (Fig. 3a), again, far beyond the previously investigated pressure region (i.e., < 2GPa).⁽²⁴⁾ Overall, all the reflections shifted to the higher 2θ angle with increasing pressure, indicating the unit cell contraction as a result of compression. The smooth evolution of the diffraction profile (i.e., no new peaks observed during the whole compression region), indicates the absence of phase transition so that N₂H₄BH₃ maintains the *Pbcn* structure at high pressures. For instance, the experimental XRD pattern at 4.45 GPa can be very well refined using the *Pbcn* structure as shown in Fig. 3b. This observation is consistent with previous high-pressure XRD study,⁽²⁴⁾ but significantly extended the phase stability region by 10 times. In addition, the XRD pattern at 20 GPa shows the profile of the crystallinity of N₂H₄BH₃ without amorphization, which suggests the high structural stability of N₂H₄BH₃. The cell parameters and crystal structures at each high pressure were refined by Rietveld method (Table S4†). The cell parameters as a function of pressure (Fig. 3d) revealed a smooth, monotonic decrease in all the cell parameters, together with the gradual reduction in the d-spacings of the 200, 211 and 400 peaks upon compression, indicating structural stability of N₂H₄BH₃ with a single *Pbcn* structure in a large pressure region.

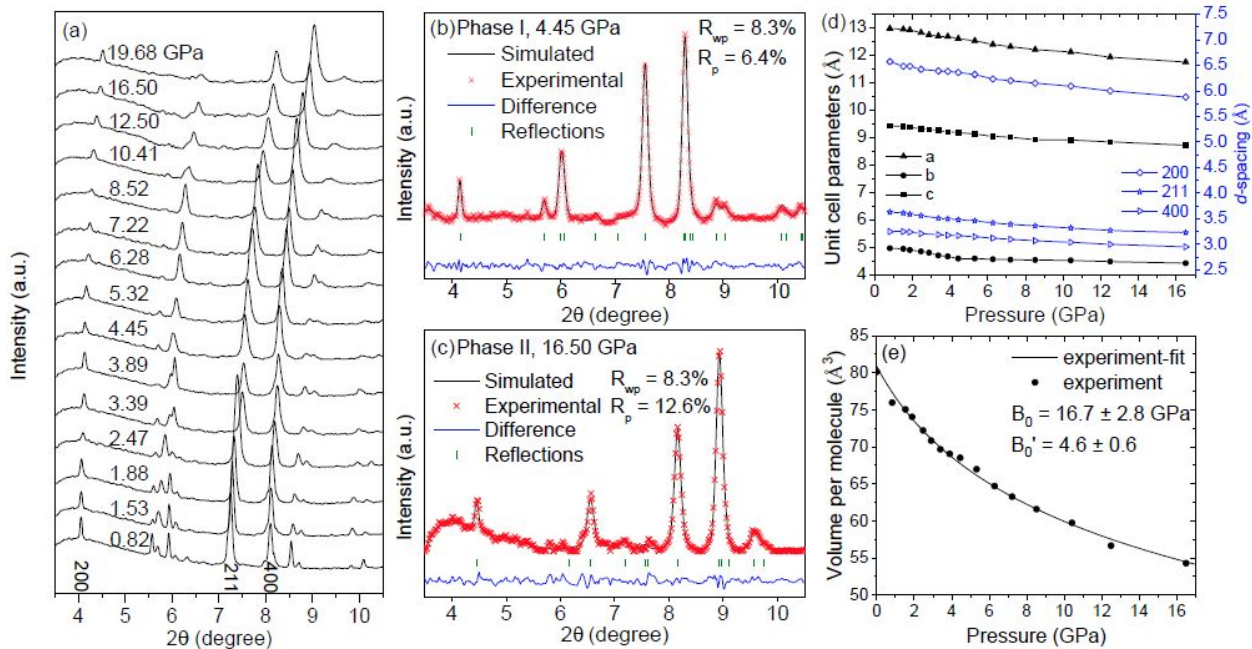


Fig. 3. (a) XRD patterns of $\text{N}_2\text{H}_4\text{BH}_3$ upon compression. Rietveld refinement of XRD patterns of $\text{N}_2\text{H}_4\text{BH}_3$ at 4.45 GPa (b) and 16.50 GPa (c) respectively. (d) Unit cell parameters (left-axis) and (200), (211), and (400) reflections (right-axis) as a function of pressure of $\text{N}_2\text{H}_4\text{BH}_3$ upon compression. (e) Experimental cell volume of $\text{N}_2\text{H}_4\text{BH}_3$ in comparison with regression using the third-order Birch–Murnaghan isothermal equation of state upon compression.

In order to address the phase stability, the compressibility of $\text{N}_2\text{H}_4\text{BH}_3$ under compression was examined by fitting the experimental unit cell volumes obtained under high pressures using the third-order Birch–Murnaghan equation of state (EOS)⁽³³⁾:

$$P(V) = \frac{3B_0}{2} \left[\left(\frac{V_0}{V} \right)^{\frac{7}{3}} - \left(\frac{V_0}{V} \right)^{\frac{5}{3}} \right] \left\{ 1 + \frac{3}{4} (B_0' - 4) \left[\left(\frac{V_0}{V} \right)^{\frac{2}{3}} - 1 \right] \right\}$$

where P is the pressure, V_0 is the reference volume, V is the deformed volume, B_0 is the bulk modulus, and B_0' is the derivative of the bulk modulus with respect to pressure. The resulting fits reveal a continuous reduction in the volume per molecule in the entire pressure range as shown in Fig. 3e. The fitted EOS parameters for experimental $\text{N}_2\text{H}_4\text{BH}_3$ were $V_0 = 80.86 \text{ \AA}^3$ per molecule

and bulk modulus $B_0 = 16.7 \pm 2.8$ GPa. This bulk modulus is slightly larger than 13.2 GPa in the previous high-pressure study probably due to the broader pressure range in this study. Compared to bulk modulus of 4.8 GPa for NH_3BH_3 and that of 7.1 GPa for ethylenediamine bisborane, the bulk modulus of $\text{N}_2\text{H}_4\text{BH}_3$ is much larger, which correlates to the higher stability of $\text{N}_2\text{H}_4\text{BH}_3$ in a relatively larger pressure region.

3.3 New high-pressure polymorphs of $\text{N}_2\text{H}_4\text{BH}_3$ revealed by DFT calculations.

To further verify the high-pressure stability of $\text{N}_2\text{H}_4\text{BH}_3$, we also performed the structure searching calculations using the USPEX package in a pressure range of 0–30 GPa. The calculations yield five top-ranked candidate structures with lowest enthalpies in four space groups labeled as follows: *Pbca*, *Pcca*, *Pmc2₁*, *Pccn* (A) and *Pccn* (B). Fig. 4a shows the calculated enthalpies of these candidate structures with pressure relative to the enthalpy of phase I (*Pbcn*). Among these structures, the enthalpy of *Pcca*, *Pmc2₁* and *Pccn* (B) increases with pressure (Fig. 4a inset) and thus these structures can be ruled out as the possible candidate for high-pressure phases. At 0 GPa, the reference *Pbcn* structure is the most stable structure among all the structures, while the enthalpy of the next most stable *Pbca* structure is only 0.014 eV/molecule higher than the *Pbcn* structure. The *Pbcn* structure remains the most stable one until around 15 GPa, when the *Pbca* structure overtakes the lead, indicating a possible phase transition from phase I (*Pbcn*) to phase II (*Pbca*). The crystal structure of phase II (*Pbca*) is shown in Fig. 4c with structural details in Table S5. In order to confirm this new phase, we employed Rietveld's method to refine the experimental XRD pattern at 16.50 GPa using the corresponding theoretical crystal structure, as shown in Fig. 3c. As can be seen, the simulated XRD pattern for phase II at 16.50 GPa using the *Pbca* structure matches the experimental data very well, which strongly supports the *Pbca* structure as a possible new high-pressure polymorph of $\text{N}_2\text{H}_4\text{BH}_3$. However, the figure of merit of refinement using the new *Pbca*

structure is merely slightly improved than using the original *Pbcn* structure indicating that *Pbcn* structure may persist at even higher pressures. Especially given the very close enthalpies between Phase I (*Pbcn*) to Phase II (*Pbca*) in the entire pressure range, we do not rule out that at above 15 GPa, *Pbcn* and *Pbca* structures may co-exist as a mixture of $\text{N}_2\text{H}_4\text{BH}_3$. Furthermore, our DFT calculations also predict another possible phase transition at 25 GPa, where the *Pccn* (A) structure (see Fig. 4d) becomes more stable than the *Pbca* structure and remains the most stable phase up to at least 30 GPa. The enthalpies of these three structures remain close to each other at pressures above 15 GPa, which indicates the possibility of the coexistence of these new phases in a broad pressure range. The comparison between experimental and theoretical volumes per molecule for $\text{N}_2\text{H}_4\text{BH}_3$ fitted using the third-order Birch-Murnaghan EOS is shown in Fig. 4b. The fitted EOS parameters for phase II were $V_0 = 80.29 \text{ \AA}^3$ and $B_0 = 10.80 \text{ GPa}$; For phase III, we obtained $V_0 = 77.48 \text{ \AA}^3$ and $B_0 = 11.61 \text{ GPa}$. These values are very comparable to those for phase I based on computed EOS, which are $V_0 = 80.70 \text{ \AA}^3$ and $B_0 = 10.31 \text{ GPa}$. We noted that above 16 GPa (Fig. 4b inset), phase II and phase III are only slightly denser than phase I where phases II and III have almost identical densities at 30 GPa. These data suggest sharp phase transitions cannot be observed which may lead to the coexistence of *Pbcn*, *Pbca* and *Pccn* (A) phases at high pressure, and that the experimental identification of new high-pressure polymorphs is highly challenging.

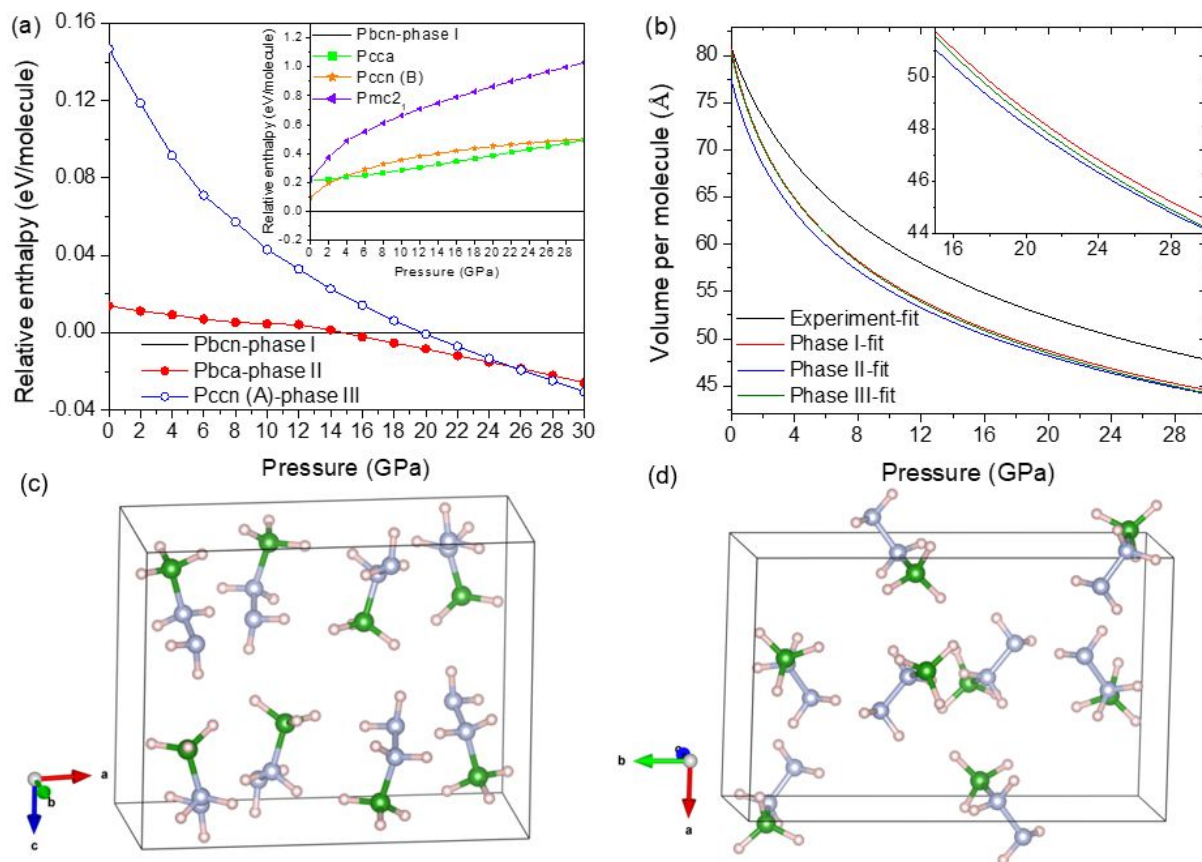


Fig. 4. (a) Enthalpy of $\text{N}_2\text{H}_4\text{BH}_3$ unit cell of candidate crystal structures as a function of pressure. (b) The third-order Birch–Murnaghan EOS fitting results for the experimental and theoretical $\text{N}_2\text{H}_4\text{BH}_4$ structures identified as phases I–III. Crystal structures of $\text{N}_2\text{H}_4\text{BH}_3$ in phase II (c) and phase III (d).

3.4 Structural stability and evolutions of dihydrogen bond of $\text{N}_2\text{H}_4\text{BH}_3$ at high pressures.

The dihydrogen bond and its pressure-tuned evolutions have been shown to have a profound impact on the structural stability and formation of new high-pressure polymorph in NH_3BH_3 and its derivatives.⁽²³⁾ The criterion of dihydrogen bonding, according to the Cambridge structural database, was established based on an empirical rule: a hydrogen bond is considered when the $\text{N-H}\cdots\text{H-B}$ distance between two molecules falls in the range from 1.7 to 2.2 Å.⁽⁴⁾ In this study, we adopted the maximum distance of 2.2 Å in order to investigate the evolution of high-pressure induced dihydrogen bonding formation process based on our DFT calculations. In addition, the

efficiency and the strength of dihydrogen bonds are also reported to be strongly influenced by the bond angles.^{4,5} In particular, N-H...H angles and H...H-B angles in the range of 89°–171° and 70°–172° respectively favors the formation of the dihydrogen bond and the evolution of dihydrogen bond angles in these ranges upon compression in all three phases were shown in Fig. S4.

At ambient pressure, four types of dihydrogen bonds that differ in bond lengths and angles are found favorable in phase I as shown in Fig. 5a. Then the number of types of dihydrogen bonds gradually increases to 10 in phase I with compression to 15 GPa (Fig. 6a), forming a stabilized framework with maximum possible dihydrogen bonds involving all BH and NH bonds in a single $\text{N}_2\text{H}_4\text{BH}_3$ molecule (Fig. 5b). At 16 GPa, the number of dihydrogen bond types in phase II becomes 11 and remains stable in the phase II region until 22 GPa where the number slightly decreases to 10 (Fig. 6b). The type of dihydrogen bonds remains 10 in phase III at 25 GPa, and then gradually increases to 12 at 30 GPa upon compression (Fig. 5c and 6c). As can be seen in Fig. 6d, the statistical average of the types of dihydrogen bonds in Phase II and III is in the range of 10–11, which can be considered relatively constant with compression.

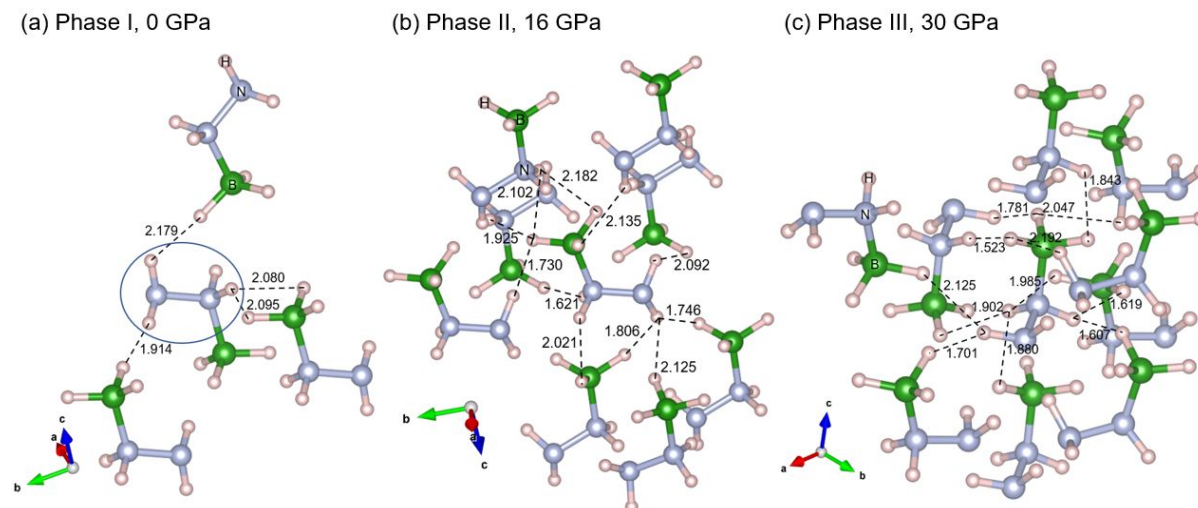


Fig. 5. Dihydrogen bonds (represented by dashed lines) in phases I (a), II (b) and III (c) at selected pressures. Each panel shows all of such bonds formed by the central molecule only.

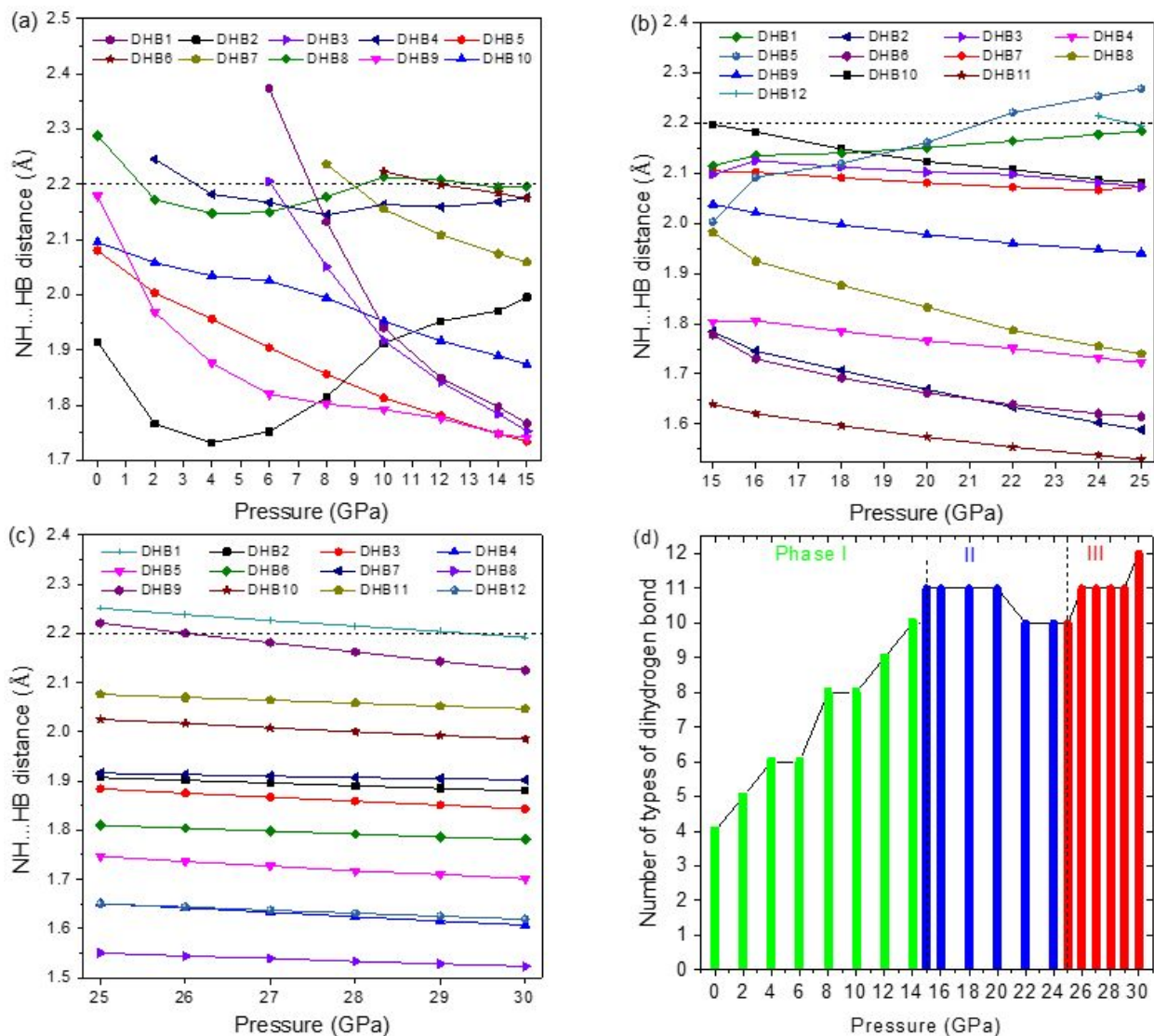


Fig. 6. Dihydrogen bond evolution as a function of pressure for phase I (a), phase II (b) and phase III (c) of $N_2H_4BH_3$. (d) The number of types of dihydrogen bonds changes upon compression.

Our studies show that $N_2H_4BH_3$ exhibits structural stability in a very broad pressure region for phase I (up to 15 GPa), in strong contrast to other NH_3BH_3 derivatives which exhibit rich pressure-induced phase transitions.^{(23),(32)} This can be understood from the starting configuration of the

dihydrogen bond and pressure-tuned evolutions in $\text{N}_2\text{H}_4\text{BH}_3$. Given the additional NH_2 group available for dihydrogen bond formation (see Fig. 5a circled N_2H_4 group where 3 out of 4 NH participates in the dihydrogen bond formation), the pre-existing dihydrogen bonds stabilized network configuration at ambient pressure allows the facile and continuous formation of dihydrogen bond to reach the maximum (i.e., 10 types) in Phase I without major structural modification. In contrast, the dihydrogen bonds in NH_3BH_3 ^{Error! Reference source not found.} are strongly disrupted (up to 50% by number) upon the first pressure-induced phase transition at ~ 1.3 GPa⁽³²⁾, whereas the number of dihydrogen bonds in ethylenediamine bisborane, a derivative of NH_3BH_3 , increases dramatically from zero to eight per molecule upon the first phase transition at ~ 1 GPa.⁽²³⁾ The correlation between pressure-tuned dihydrogen bonds and structural stability (vs. phase transitions) strongly suggests that the pre-existing dihydrogen bonds in $\text{N}_2\text{H}_4\text{BH}_3$ play a very minor role in pressure-induced structural changes leading to a large structural stability region.

Then other structural factors need to be examined as the possible driving force for the pressure-induced polymorphic transitions at higher pressures. In particular, both NH_3BH_3 and ethylenediamine bisborane exhibit a relatively large and distinctive volume collapse during the phase transitions indicating a significant contribution from the P-V term as the thermodynamic driving force for the phase changes. In contrast, the volume change in $\text{N}_2\text{H}_4\text{BH}_3$ is very small for both the phase transitions upon compression, with no observable volume collapse (Fig. 4b). This observation is consistent with the observation that in both phase transitions at 15 and 25 GPa for $\text{N}_2\text{H}_4\text{BH}_3$ the dihydrogen bond changed merely incrementally or exhibited no change. Therefore, we conclude that the possible polymorphic transitions at 15 and 25 GPa are second order in nature with dihydrogen bonds playing a negligible role in the pressure-induced phase transition in $\text{N}_2\text{H}_4\text{BH}_3$.

Furthermore, the DFT calculated enthalpies of phase I and phase II remain very close to each other in the entire pressure range of 0–20 GPa, and the enthalpy of phase II and phase III remain very close as well throughout 20 to 30 GPa (see Fig. 4a). These results show that the predicted high-pressure phases (II and III) are not significantly thermodynamically more favorable than the ambient pressure phase without additional dihydrogen bond contributions. Coincidentally, the structure searching calculations on $\text{N}_2\text{H}_4\text{BH}_3$ yielded a very limited number of stable candidate structures under a wide pressure range, in strong contrast to the highly diversified suitable structures found for ethylenediamine bisborane where the same searching algorithm was employed.⁽²³⁾ Error! Reference source not found.

Overall, $\text{N}_2\text{H}_4\text{BH}_3$ exhibits an unprecedented structural stability over a broad pressure range with very few distinctive high-pressure polymorphs. Given the initial high hydrogen content and relatively low dehydrogenation temperature (i.e., ~ 60 °C) which already makes $\text{N}_2\text{H}_4\text{BH}_3$ a desirable hydrogen storage candidate, pressure may further enhance its dehydrogenation performance. In particular, pressure can enhance the dihydrogen bond interaction in the framework, constrain the specific molecular stacking thus facilitating the formation of the oligomeric solid product, and even suppress the formation channels of N_2H_4 and NH_3 as byproducts,⁽¹⁷⁾ all favorable to enhance the dehydrogenation yield and kinetics. Given the high-pressure structural stability of $\text{N}_2\text{H}_4\text{BH}_3$, it would be interesting to characterize the dehydrogenation process *in situ* in a broad, controlled pressure-temperature range. This knowledge will be very valuable for the understanding of dehydrogenation mechanisms and thus for the design of new hydrogen storage materials.

4. Conclusions

In summary, we report the structural stability and pressure-induced polymorphic transitions in $\text{N}_2\text{H}_4\text{BH}_3$, a promising hydrogen storage material, using *in situ* vibrational spectroscopy and

synchrotron X-ray diffraction aid with DFT calculations. We discovered that the ambient pressure structure of *Pbcn* remains stable up to 15 GPa (phase I). At pressures higher than 15 GPa, compression of $\text{N}_2\text{H}_4\text{BH}_3$ induces two phase transitions: the first one from phase I to a *Pbca* structure (phase II) near 15 GPa, and the second one at about 25 GPa, from phase II to a *Pccn* structure (phase III). The identifications of these transitions are supported by the structural refinement with XRD patterns combined with relative enthalpies predicted by DFT calculations. The investigation of the N–H···H–B dihydrogen bond network evolution of $\text{N}_2\text{H}_4\text{BH}_3$ upon compression sheds light on the origin of the structural stabilities of phase I and the nature of the polymorphic transitions at higher pressures. In contrast to many previously reported high-pressure structures of ammonia borane derivatives, we found that the dihydrogen bonds although abundant in all phases of $\text{N}_2\text{H}_4\text{BH}_3$, do not play an important role in the pressure-induced phase transitions of $\text{N}_2\text{H}_4\text{BH}_3$. These findings demonstrate the unprecedented stability of $\text{N}_2\text{H}_4\text{BH}_3$ that allows further investigation of dehydrogenation mechanisms in a broad P-T range. Therefore, our work provides additional insights into the application of $\text{N}_2\text{H}_4\text{BH}_3$ as a hydrogen storage material.

Acknowledgement

This work was supported by a Discovery Grant, a Research Tools and Instruments Grant from the Natural Science and Engineering Research Council of Canada, a Leaders Opportunity Fund from the Canadian Foundation for Innovation. The synchrotron XRD was performed sector 20ID, Advanced Photon Source (APS), Argonne National Laboratory (ANL). The APS is an Office of Science User Facility operated for the U.S. Department of Energy (DOE) Office of Science by ANL and was supported by the U.S. DOE under Contract No. DE-AC02-06CH11357, and the Canadian Light Source and its funding partners. The calculations were partially supported by the

facilities of the Shared Hierarchical Academic Research Computing Network (SHARCNET: www.sharcnet.ca) and Compute/Calcul Canada.

Reference

- (1) A. Schneemann, J. L. White, S. Kang, S. Jeong, L. F. Wan, E. S. Cho, T. W. Heo, D. Prendergast, J. J. Urban, B. C. Wood, M. D. Allendorf and V. Stavila, *Chem. Rev.*, 2018, **118**, 10775–10839.
- (2) R. Kumar, A. Karkamkar, M. Bowden and T. Autrey, *Chem. Soc. Rev.*, 2019, **48**, 5350–5380.
- (3) A. Staubitz, A. P. M. Robertson and I. Manners, *Chem. Rev.*, 2010, **110**, 4079–4124.
- (4) T. Richardson, S. de Gala, R. H. Crabtree and P. E. Siegbahn, *J. Am. Chem. Soc.*, 1995, **51**, 12875–12876.
- (5) W. T. Klooster, T. F. Koetzle, P. E. M. Siegbahn, T. B. Richardson and R. H. Crabtree, *J. Am. Chem. Soc.*, 1999, **121**, 6337–6343.
- (6) Y. Huang, L. Ji, L. Shi, H. Ren, Z. He and G. Ji, *J. Phys. Chem. C*, 2020, **124**, 27300–27308.
- (7) Y. Lin, W. L. Mao and H. Mao, *Proc. Natl. Acad. Sci. U. S. A.*, 2009, **106**, 8113–8116.
- (8) S. Xie, Y. Song and Z. Liu, *Can. J. Chem.*, 2009, **87**, 1235–1247.
- (9) A. Liu and Y. Song, *J. Phys. Chem. C*, 2012, **116**, 2123–2131.
- (10) Y. Liang and J. S. Tse, *J. Phys. Chem. C*, 2012, **116**, 2146–2152.
- (11) Y. Lin, H. Ma, C. W. Matthews, B. Kolb, S. Sinogeikin, T. Thonhauser and W. L. Mao, *J. Phys. Chem. C*, 2012, **116**, 2172–2178.
- (12) Y. Yao, X. Yong, J. S. Tse and M. J. Greschner, *J. Phys. Chem. C*, 2014, **118**, 29591–29598.
- (13) H. Liu, C. Liu, Q. Li, Y. Ma and C. Chen, *J. Phys. Chem. Lett.*, 2021, **12**, 2036–2043.
- (14) S. Nakano, F. Hiroshi, Y. Hiroshi and T. Kikegawa. *J. Chem. Phys.*, 2022, **157**, 234702.

- (15) B. Peng and J. Chen, *Energy Environ. Sci.*, 2008, **1**, 479–483.
- (16) J. Goubeau and E. Ricker, *Z. Anorg. Allg. Chem.*, 1961, **310**, 123–142.
- (17) R. Moury, G. Moussa, U. B. Demirci, J. Hannauer, S. Bernard, E. Petit, A. van der Lee and P. Miele, *Phys. Chem. Chem. Phys.*, 2012, **14**, 1768–1777.
- (18) R. Moury and U. B. Demirci, *Energies*, 2015, **8**, 3118–3141.
- (19) T. Hügler, M. F. Kühnel and D. Lentz, *J. Am. Chem. Soc.*, 2009, **131**, 7444–7446.
- (20) Y. Song, *Phys. Chem. Chem. Phys.*, 2013, **15**, 14524–14547.
- (21) A. Torabi, Y. Song and V. N. Staroverov, *J. Phys. Chem. C*, 2013, **117**, 2210–2215.
- (22) A. Torabi, C. Murli, Y. Song and V. N. Staroverov, *Sci. Rep.*, 2015, **5**, No. 13929.
- (23) R. Guan, P. Wang, Y. Song and V. N. Staroverov, *J. Phys. Chem. C*, 2021, **125**, 18614–18622.
- (24) P. G. Yot, V. Yadav, S. O. Amara, J. P. Itie, U. B. Demirci and G. Maurin, *Phys. Chem. Chem. Phys.*, 2018, **20**, 2845–2850.
- (25) B. H. Toby and R. B. Von Dreele, *J. Appl. Crystallogr.*, 2013, **46**, 544–549.
- (26) S. J. Clark, M. D. Segall, C. J. Pickard, P. J. Hasnip, M. I. Probert, K. Refson and M. C. Payne, *Z. für kristallogr. – cryst. Mater.*, 2005, **220**, 567–570.
- (27) S. Mebs, S. Grabowsky, D. Förster, R. Kickbusch, M. Hartl, L. L. Daemen, W. Morgenroth, P. Luger, B. Paulus and D. Lentz, *J. Phys. Chem. A*, 2010, **114**, 10185–10196.
- (28) A. R. Oganov and C. W. Glass, *J. Chem. Phys.*, 2006, **124**, No. 244704.
- (29) A. R. Oganov, A. O. Lyakhov and M. Valle, *Acc. Chem. Res.*, 2011, **44**, 227–237.
- (30) J. P. Perdew, K. Burke and M. Ernzerhof, *Phys. Rev. Lett.*, 1996, **77**, 3865–3868.
- (31) H. J. Monkhorst and J. D. Pack, *Phys. Rev. B*, 1976, **13**, 5188–5192.

- (32) N. Satoshi, A. Sano-Furukawa, T. Hattori, S. Machida, K. Komatsu, H. Fujihisa, H. Yamawaki, Y. Gotoh and T. Kikegawa. *Inorg. Chem.*, 2021, **60**, 3065–3073.
- (33) F. Birch, *Phys. Rev.*, 1947, **71**, 809–824.